Universiteit Utrecht

Utrecht University

DEPARTMENT OF EARTH SCIENCES

MASTER OF SCIENCE THESIS

23 May 2018

Subsurface Reflection and Transmission Response Estimation by Seismic Interferometry Using Deep Borehole Data at Groningen

Muhammad Fadhillah Akbar

Supervised by:
Dr. Ivan Pires de Vasconcelos
Department of Earth Sciences, Utrecht University

Dr. Hanneke Paulssen
Department of Earth Sciences, Utrecht University

Abstract

Seismic interferometry reconstructs the impulse response between two receivers. In this study, we use deconvolution interferometry to estimate the subsurface reflection and transmission response using active and passive borehole data in the Groningen gas reservoir at ~3 km depth. Assuming the medium is approximately laterally homogeneous, recorded up- and downgoing P- and S-wave are separated using f-k filtering based on wavenumber and velocity. We validate the wavefield separation and deconvolution interferometry process using synthetic data of a 1D elastic model built from field P-wave velocity logging. The estimated full-waveform reflection response using a virtual source at the top geophone is consistent with the actual response from synthetic data with a corresponding active source. For the virtual source at the bottom geophone, the reflection response appears to be phase delayed, though its arrivals are consistent with the local subsurface geology. Using the same principle, a first-order estimated local transmission response successfully approximates the P-wave velocity in the reservoir. We show that seismic interferometry in a deep borehole setting can retrieve the physical reflection response and velocity structure in the reservoir. Reliable subsurface information obtained from borehole interferometry can be of use for reservoir imaging without requiring knowledge of the medium parameters, and for reservoir monitoring by detecting velocity and/or interface time-lapse variations with negligible cost and effort compared to conventional approaches.

Keywords: seismic interferometry, deconvolution, up-down separation, reflection response, transmission response, borehole.

Table of Contents

1 Introduction

Seismic interferometry is a proven method to estimate the impulse response between two receivers as if one receiver acts as a virtual source and the other receiver observes the response. The main strength of this method is that it requires no knowledge of medium parameters nor of the position or timing of the actual source, so long as the wave comes from sources in Fresnel zones around stationary points (Wapenaar et al., 2010).

Discovered in 1959 and started production in 1963, the Groningen gas field in the Netherlands has been one of the most prolific natural gas fields. Vast gas extraction has caused subsidence and increase in induced seismicity (van Thienen-Visser & Breunese, 2015). In 2013, a geophone array which covers almost the entire thickness of reservoir at ~3 km depth was placed in borehole SDM-1 for micro-seismic monitoring (NAM, 2016). Aside from recording noise data, check shots at the surface were recorded to calibrate the geophone orientation. Zhou & Paulssen (2017) determined the P- and S-wave velocity structure along the reservoir using noise interferometry by cross-correlation and inferred that the source is mainly anthropogenic surface noise.

In this study, we use deconvolution interferometry to estimate the transmission and reflection response using SDM-1 borehole data, with a virtual source at the top or bottom geophone. This can be achieved by up- and downgoing wavefield separation in f-k domain prior to deconvolution. As in our case, Vasconcelos & Snieder (2008) suggested that deconvolution is of most use for interferometry application with complicated source signal (man-made noise, natural noise) and/or involving wavefield separation. The main objective is to show that deconvolution interferometry using check shot and noise borehole data can estimate; a) The transmission response which corresponds to the velocity structure in the reservoir, and b) The physical reflection response within and around the reservoir. We validate the process by applying it first to the synthetic data from the 1D elastic model by Chen (2017) obtained from well log data by NAM (Nederlandse Aardolie Maatschappij).

1.1 Seismic interferometry by deconvolution

In interferometry, Green's function or impulse response retrieval is typically done by crosscorrelation of responses at two receiver locations (Wapenaar et al., 2010; Curtis et al., 2016). Wapenaar & Fokkema (2006) mathematically derived the Green's function representation obtained from seismic interferometry. Although it yields an accurate representation of waves propagating between receivers, the product of cross-correlation does not yield only the impulse response. The power spectrum of the source function leaves an imprint on the estimated impulse response if not properly resolved (Wapenaar et al., 2010). It is often difficult if the source function is complex or unknown such as in the case of anthropogenic and natural noise. Another option for interferometry is to use deconvolution. Deconvolution interferometry yields an impulsive response without the need of independent estimate of the source function (Vasconcelos & Snieder, 2008) and eliminates its imprint on the impulse response. It has been used to estimate near-surface velocities (Mehta et al., 2007) and deep local imaging (Liu et al., 2014) in borehole configuration. Vasconcelos & Snieder (2008) described its application for drill-bit seismic imaging.

Interferometry by water-level regularized deconvolution of two records of receivers at locations x_R and x_S in the frequency domain (w) is expressed by

$$\widehat{D}(x_R, x_S, w) = \frac{\hat{p}(x_R, w)\hat{p}^*(x_S, w)}{|\hat{p}(x_S, w)|^2 + \varepsilon^2} \qquad (1)$$

where $\widehat{D}(x_R, x_S, w)$ is the response at receiver x_R of a virtual source at receiver x_S. As the input, $\hat{p}(x_R, w)$ and $\hat{p}(x_S, w)$ are the recordings at x_R and x_S. The asterisk denotes complex conjugation. ε^2

is a stabilization parameter. In this study we choose ε^2 to be 1% of the maximum spectral power of $\hat{p}(x_S, w)$.

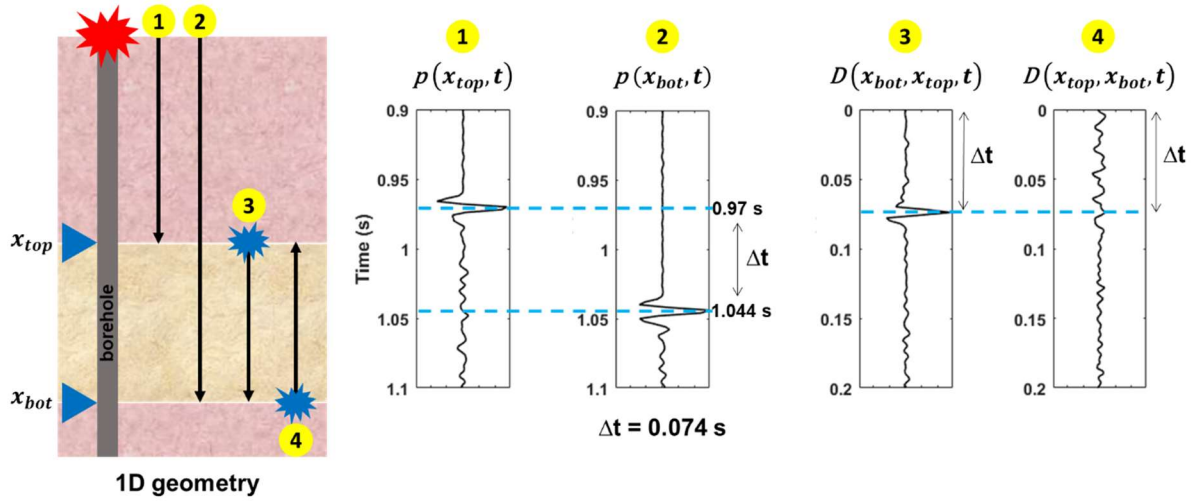

Figure 1 *Illustration of 1D seismic interferometry with a synthetic active source at the surface. Black arrow depicts a wave path from the corresponding source. x is the geophone location at the top and bottom (subscripts top and bot). 1) Response observed by geophone at x_{top} from excitation at the surface. 2) Response observed by geophone at x_{bot} from excitation at the surface. 3) Estimated response observed at x_{bot} as if we have a virtual source at x_{top}. 4) Estimated response observed at x_{top} as if we have a virtual source at x_{bot}.*

Fig. 1 illustrates the concept of 1D seismic interferometry using synthetic borehole data with an active source at the surface. All quantities in Fig. 1 are in the time domain (t). $p\left(x_{top}, t\right)$ and $p\left(x_{bot}, t\right)$ are seismic responses observed at the geophone located at the top (x_{top}) and bottom (x_{bot}) respectively, from excitation of active source at the surface (red explosion). With the top and bottom geophone have a certain distance, the first arrival observed by each geophone would have a time delay (Δt) which is affected by the medium between the two geophones. The delay time of the first arrival between the two geophones is 0.074 s.

In principle, by interferometry, one can estimate the response observed at one of the geophones as if the other acts as a virtual source (blue explosion), without the knowledge of medium between receivers. Bakulin & Calvert (2006) showed that virtual source method can image structure below complex overburden without the need of velocity model. $D\left(x_{bot}, x_{top}, t\right)$ is the estimated response observed at the bottom geophone from virtual source at the top geophone. $D\left(x_{top}, x_{bot}, t\right)$ is the estimated response observed at the top geophone from a virtual source at the bottom geophone. In theory, the first arrival time estimated from interferometry is equal to the delay time of the actual first arrivals between two geophone recording. This is the case for a virtual source at the top geophone where the first arrival comes at exactly 0.074 s. As for virtual source at the bottom geophone, though it arrives at 0.074, the first arrival amplitude does not stand out compared to non-physical event at earlier time. This first arrival picking is based on observation of the whole seismic section before choosing the first arrival at that particular trace.

Events prior to the first arrivals are non-physical events. It is clear that with a virtual source at the bottom geophone, the non-physical events are stronger especially before the first arrival, indicating that the response estimation is less stable compared to a virtual source at the top geophone as will be described in Chapter 3.2. Despite the downside of virtual source at the bottom geophone, we see that interferometry can approximate the impulse response between two receivers without the knowledge of the medium parameter between the geophones, nor the location and the timing of the actual source at

the surface. Although in this example we use interferometry by deconvolution, in practice it can also be illustrated using cross-correlation.

1.2 Reflection and transmission response estimation

To estimate the reflection responses, we follow the equation by Vasconcelos et al. (2017) with regularized deconvolution. R are reflection responses with virtual sources either at the top (R^+) or bottom (R^-). p^+ and p^- are the downgoing and upgoing waves recorded at the top, or at the bottom geophone (subscripts *top* and *bot*). All quantities are in frequency domain. For a virtual source at the top geophone, R^+ can be interpreted as the estimated upgoing responses from a downgoing impulse excitation at the top geophone, recorded by other geophones (equation 2). The same concept also applies for a virtual source at the bottom geophone. The estimated R^- are the downgoing reflected responses from an upgoing impulse excitation at the bottom geophone, recorded by other geophones (equation 3). The estimated reflection response is not only locally within the reservoir, but also targeting the responses from interfaces in the medium above and below the reservoir.

$$p_{top}^- = R^+ p_{top}^+ \quad (2), \qquad p_{bot}^+ = R^- p_{bot}^- \quad (3),$$

$$p_{bot}^+ = T_{TE}^+ p_{top}^+ + R_{TE}^- p_{bot}^- \quad (4), \qquad p_{top}^- = T_{TE}^- p_{bot}^- + R_{TE}^+ p_{top}^+ \quad (5)$$

As for local, reservoir-only transmission responses, we use equations 4 and 5 to incorporate artifacts on the transmission wave coda (Vasconcelos et al., 2017). T_{TE} and R_{TE} are local (target-enclosing) transmission and reflection responses with virtual sources either at the top or bottom (superscripts + and -), as if there is no medium above and below the reservoir. For a virtual source at the top geophone, T_{TE}^+ can be interpreted as the estimated downgoing responses from a downgoing impulse excitation at the top geophone, recorded by other geophones (equation 4). For a virtual source at the bottom geophone, the estimated T_{TE}^- are the upgoing responses from an upgoing impulse excitation at the bottom geophone, recorded by other geophones (equation 5). Note that by deconvolving equation 4 or 5 with p_{top}^+ or p_{bot}^- according to the chosen virtual source location to determine T_{TE}^+ or T_{TE}^-, the second term in the right side of the equation is not eliminated, which corresponds to the artifact of spurious waves from the medium above and below the reservoir. Therefore, the transmission response estimation in this study is a superposition of the local transmission and these artifacts. Fig. 2 illustrates the transmission and reflection response estimation by deconvolution interferometry. It is possible that the reflection and transmission response contains waves that reflected multiple times.

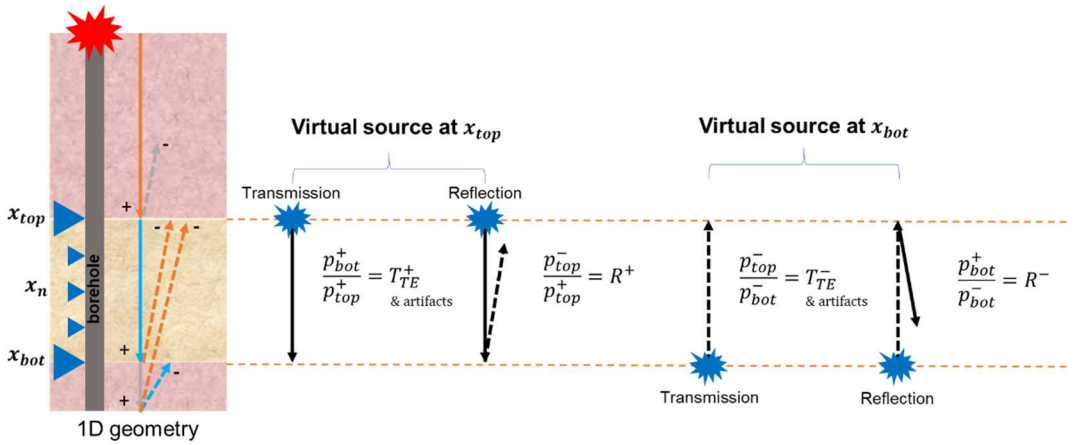

Figure 2 *Reflection and transmission response illustration by deconvolution interferometry with an active source at the surface (red explosion) and virtual source at the top and bottom geophone (blue explosions). The solid and dashed lines indicate the down- and upgoing waves. Orange and light blue lines portray wave paths that are recorded at* x_{top} *and* x_{bot} *(both up- and downgoing wave).*

As expressed by equation 1 to 4, the reflection and transmission estimation method requires separated up- and downgoing waves as the input for deconvolution interferometry. Without wavefield separation, full waveform interferometry can obtain reflected waves superimposed with the direct arrival (first-order transmission wave), their coda, and artifacts such as spurious arrivals (Snieder et al., 2006). Zhou & Paulssen (2017) identified these events using cross-correlation interferometry. In this research, we separately estimate the reflection and transmission response by up- and downgoing wavefield separation in the f-k domain. Up-down separation prior to interferometry can suppress the artifacts of spurious arrivals from overburden medium and limited acquisition aperture, therefore, improves the signal-to-noise ratio (Mehta et al., 2007).

1.3 Up- and downgoing wavefield separation

Each geophone records up- and downgoing waves corresponding to their propagation direction along the array (Fig. 2). The up- and downgoing P and S-wave separation are achieved by f-k filtering. We separate the up- and downgoing wave propagation by their wavenumber (k). Because the medium is approximately laterally homogeneous (Fig. 4), upgoing waves have negative k and downgoing waves have positive k (Fig. 3). P and S-wave separation is achieved by slope filters in the f-k domain where the slopes correspond to wave velocities, which are estimated from well-log information over the same depth interval.

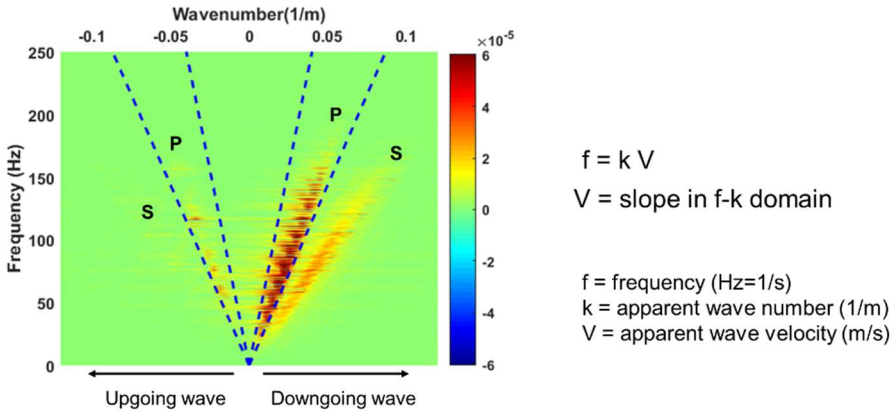

Figure 3 *Up- and downgoing wavefield separation in the f-k domain using synthetic data. The area inside the blue dashed line represents the P-wave energy that we pass. The slope of the dashed line is based on the chosen Vp limit.*

Fig. 3 shows the up- and downgoing P and S-wave f-k spectrum from the synthetic response of an active source at the surface. It clearly shows that we can distinguish the up- and downgoing P- and S-wave based on their slope and k. Blue dashed lines represent the minimum and maximum P-wave velocity based on the well-log information. The up- and downgoing wave are separated by filtering the unwanted k. The same principle of wavefield separation is applicable to the check shot and noise data. The separated up- and downgoing P-waves from f-k filtering are used as the input for deconvolution interferometry.

1.4 Overview of geology and research objective

The reservoir in Groningen gas field is the Rotliegend sandstone at ~2769 – 3040 m depth covered by a thin layer of basal anhydrite followed by thick Zechstein salt formation. Below the reservoir is the Carboniferous claystone formation (Fig. 4). Two deep geophone arrays (SDM-1 and ZRP-1) are placed in Loppersum area to monitor the seismicity in the reservoir. We use SDM-1 borehole data in which the geophone array covers almost the entire thickness of the reservoir. The array consists of 10 geophones that are aligned almost vertically. Lateral changes in the reservoir around SDM-1 well are relatively small.

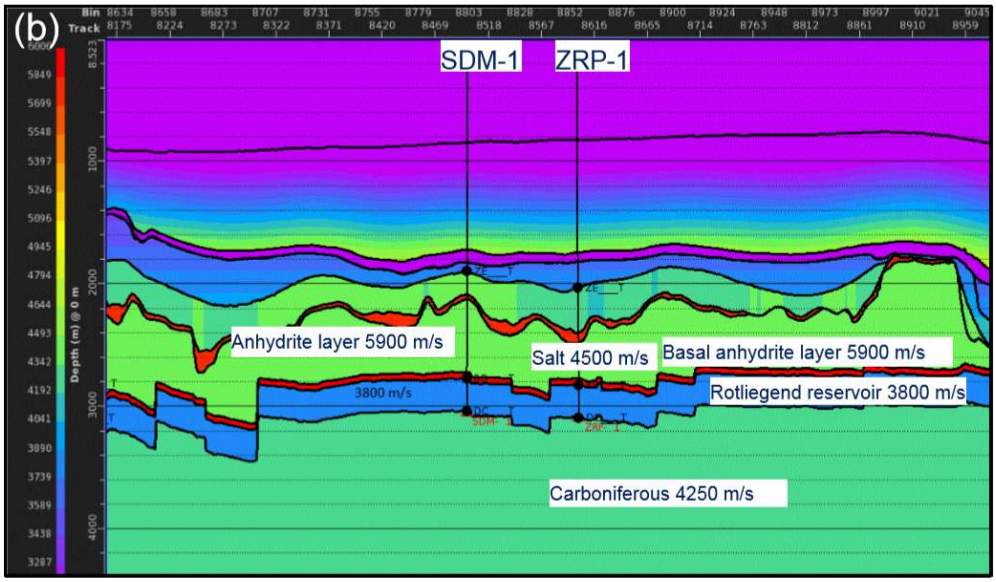

Figure 4 *Overview of the geology in the SDM-1 well proximity (Zhou & Paulssen, 2017). The target of micro-seismic monitoring is the Rotliegend gas reservoir, flanked by basal anhydrite layer and Carboniferous formation at the top and bottom.*

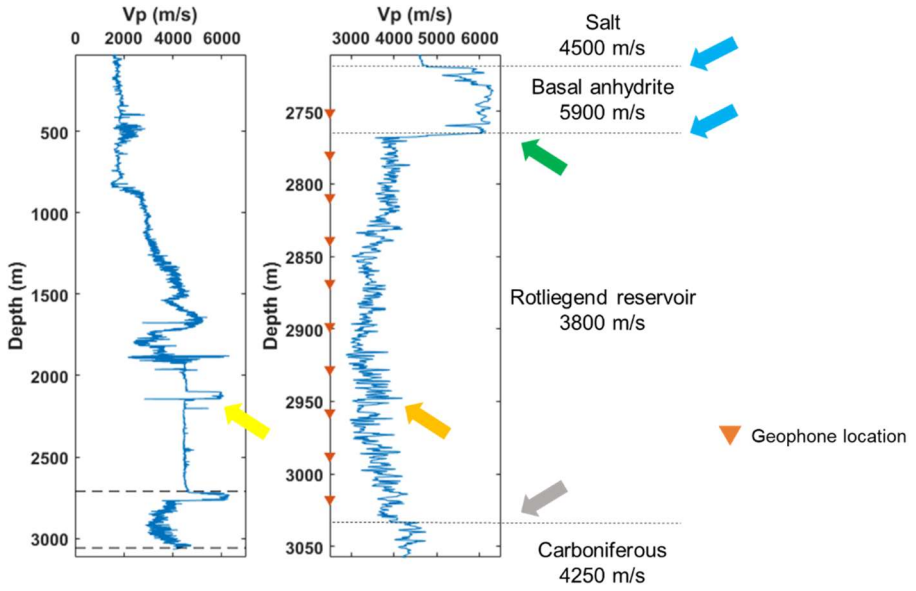

Figure 5 *SDM-1 compressional velocities (Vp). Left: Overall Vp log. Right: Local Vp log within and around the reservoir.*

The aim of this research is to estimate the physically meaningful reflection response from actual subsurface interfaces within and around the reservoir. The interface corresponds to a high change in velocity due to changes in rock formation (Fig. 5). Two major interfaces as our target are the contact between formation at the top and bottom of the Rotliegend reservoir (green and grey arrow). With a virtual source set at the top or bottom geophone, we expect these interfaces would produce a prominent reflection wave. Two close interfaces at the top and bottom of a thin basal anhydrite layer (blue arrow) are expected to be resolved in synthetic data where we have a high-frequency content, therefore small enough wavelength to sample these interfaces. As for check shot and noise data with much lower frequency content, these close interfaces are expected to be poorly resolved. For transmission response estimation, the aim is to approximate the ballistic-wave velocities structure within the reservoir. The reservoir itself contains velocity heterogeneities which would also influence the result of estimated reflection and transmission response.

2 Data processing

The check shot and noise data of the SDM-1 borehole are recorded by 3-C geophone with a sampling rate of 2000 Hz. A total of 10 geophones with 30 m spacing are placed at 2750 – 3017 m depth. We use 4 check shot data with a 30 sec record each. For noise data, we use a 24 hours record (21 November 2013) divided into 2880 records of 30 sec record each. We use only the vertical component of data which has the strongest P wave.

We apply processing sequences as in Fig. 6. Check shot and noise data is resampled to 250 Hz because the frequency content of the signal is only up to ~80 Hz. Resampling is not applied to the synthetic data. Even though the data contain frequencies up to 80 Hz, the data are aliased due to very low spatial sampling. Aliasing is easily identified as wraps around in f-k plot (Fig. 7a). Hence, the band-pass filter of 5.5 – 37 Hz is applied prior to f-k filtering to suppress aliased signals and to remove very low-frequency noise (Fig. 7b and 8). Band-pass filtering also produces minor artifacts above the first arrival which, although insignificant, would affect further processing sequences.

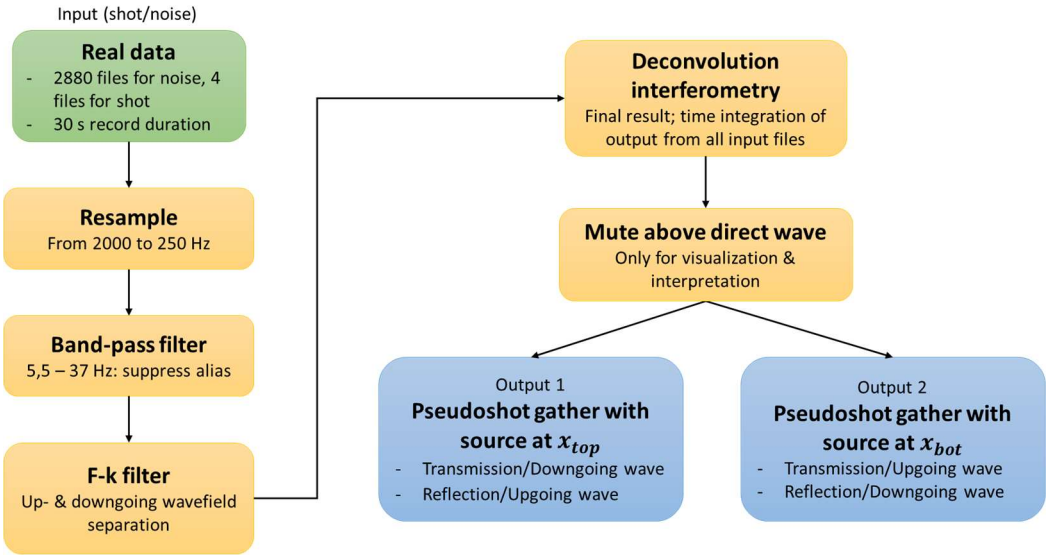

Figure 6 *Processing flowchart of transmission and reflection response estimation using interferometry with a virtual source at the top (output 1) and bottom geophone (output 2).*

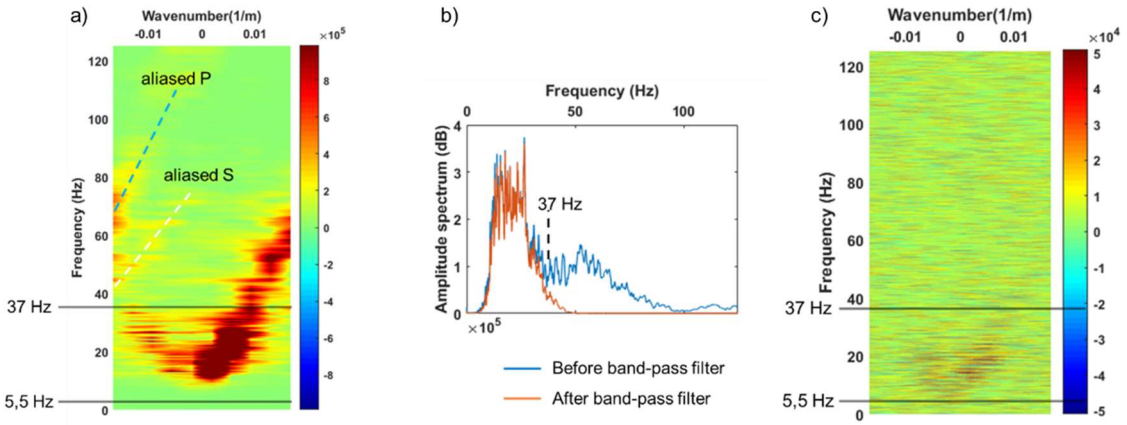

Figure 7 *F-k analysis of check shot and noise data. a) F-k plot shows wraps around indicating aliased signal. b) Frequency content of check shot data before and after the band-pass filter to suppress aliasing. c) F-k plot of noise data. Its spectrum distribution resembles the check shot data.*

Noise data are processed the same way as the check shot assuming the source of noise only comes from above or below (Zhou & Paulssen, 2017). Indeed, f-k analysis of noise data shows that their spectrum resembles the check shot with the downgoing wave dominating over the upgoing wave, except with a narrower band and weaker energy (Fig. 7c). This confirms that the noise is predominantly originated from above.

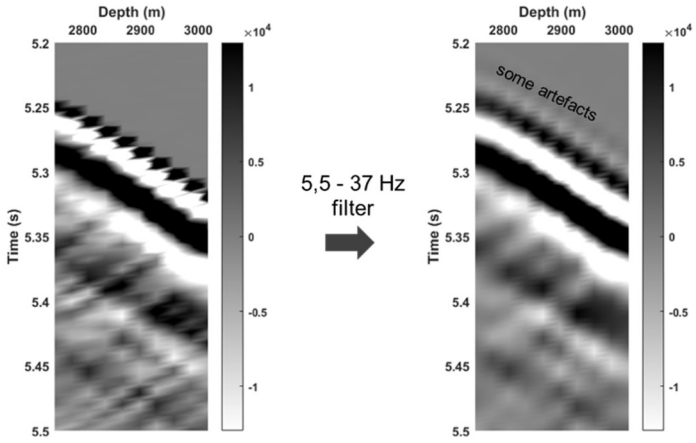

Figure 8 *Check shot data before and after the band-pass filter. Although reducing aliasing, it introduces minor artifact above the first arrivals.*

After band-pass filter, up- and downgoing wavefield separation in f-k domain and time integration of deconvolution interferometry is applied to estimate reflection and transmission wave for a virtual source at the top and bottom geophone. For easier interpretation of reflection response, non-physical events and artifacts above first arrivals are muted based on the well-log information.

3 Synthetic data

To validate the process, the processing sequence in Fig. 6 is first applied to the synthetic data from the 1D elastic model by Chen (2017). In the synthetic data, 9 additional geophones are placed between the real geophone locations to prevent aliasing and misinterpretation. A total of 91 geophones gives enough spatial sampling to clearly investigate and parameterize the process. A Ricker wavelet with a peak frequency of 80 Hz is used to generate a synthetic response. The incident angle is set to zero. The S-wave velocity (*Vs*) is simplified to be half of the *Vp*.

With the available 1D model, synthetic responses from a physical active source at the top and bottom geophone are generated. These are to be compared with the estimated response from deconvolution interferometry with a virtual source at the top and bottom geophone to validate the deconvolution process. The model also made it possible to generate only the up- or downgoing synthetic response for a physical active source at the surface to be compared with the up- and downgoing wave from f-k filtering outputs, therefore validating the wavefield separation process.

3.1 Wavefield separation in synthetic data

Fig. 9a shows the up- and downgoing P- and S-waves from the synthetic response and its f-k spectrum. We pass the P-wave with *Vp* of 2877 – 6249 m/s (blue dashed lines) based on the well-log information. Fig. 9b and 9c show the down- and upgoing P-wave and its corresponding f-k spectrum after wavefield separation in the f-k domain. S-wave is successfully filtered out on both results. For comparison, Fig. 10b and 10d show up- and downgoing waves generated directly from the model. Up- and downgoing

waves resulting from f-k filtering (Fig. 10a and 10c) are in good agreement with the up- and downgoing waves from the model, which validates the wavefield separation process. Note the f-k filtering inability to fully recover the changes of slope in seismic events due to velocity variation at the seismic section boundary (red dashed circle). This is because of spatial limitation of the data, which are not available infinitely in space.

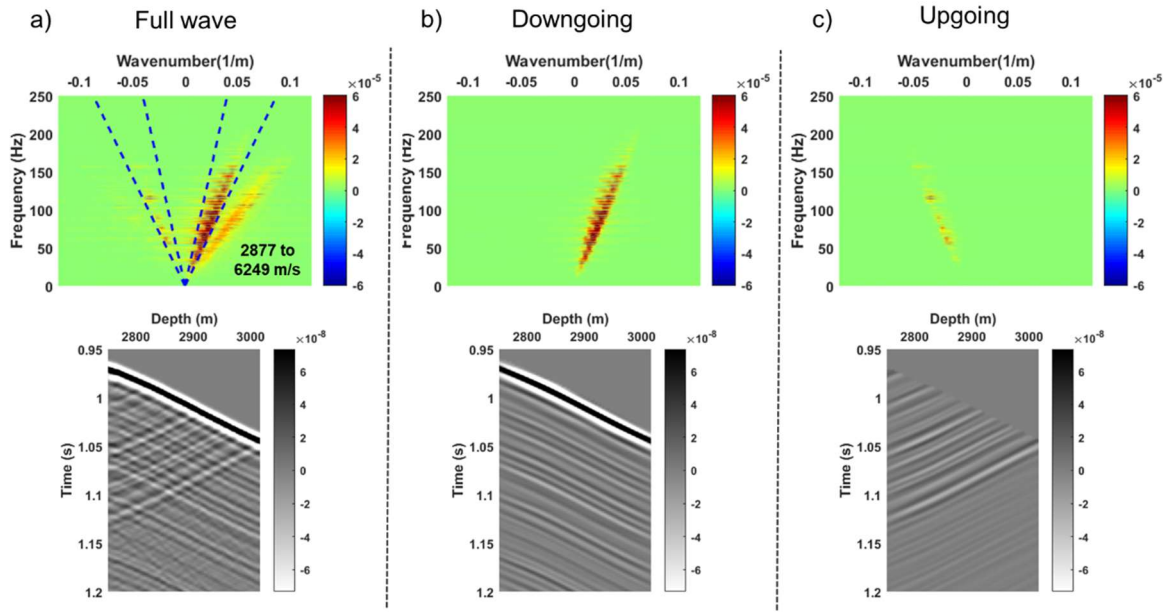

Figure 9 *Wavefield separation of synthetic shot data in the f-k domain with a physical source at the surface. a) The up- and downgoing wave and its f-k spectrum. b) Downgoing wave and its f-k spectrum. c) Upgoing wave and its f-k spectrum.*

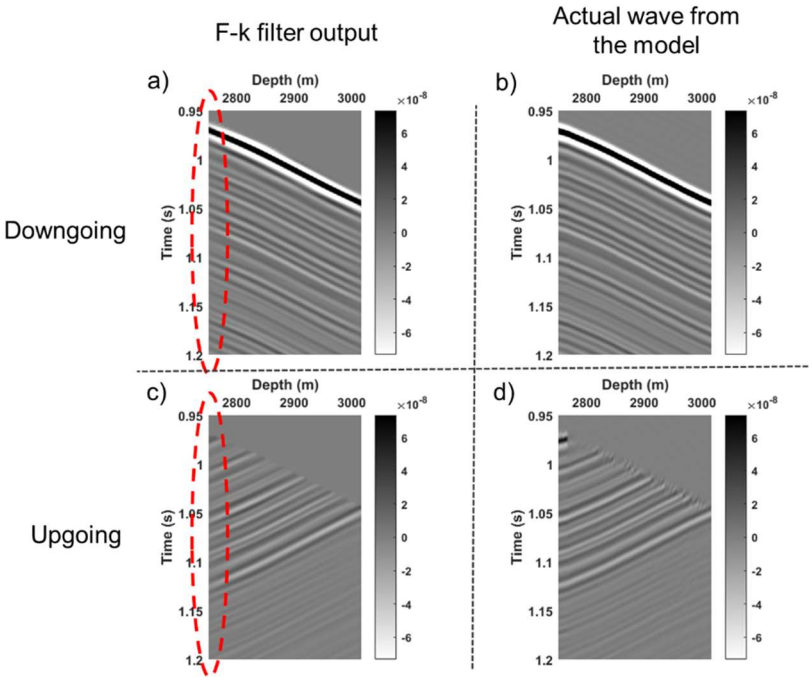

Figure 10 *F-k filter outputs compared with the up- and downgoing wave generated by the model. a) and b) are the downgoing wave from the f-k filter and the model respectively. c) and d) are the upgoing wave from the f-k filter and the model respectively.*

3.2 Reflection and transmission response estimation from synthetic data

First, we validate the reflection and transmission response estimation by using synthetic shot data after wavefield separation. The deconvolution interferometry results are compared with the actual waves from 1D synthetic truncated model as if there is an active source at the top and bottom geophone location. For a virtual source at the top geophone, the model is truncated as if there is no medium above the virtual source. For a virtual source at the bottom geophone, the model is truncated as if there is no medium below the virtual source.

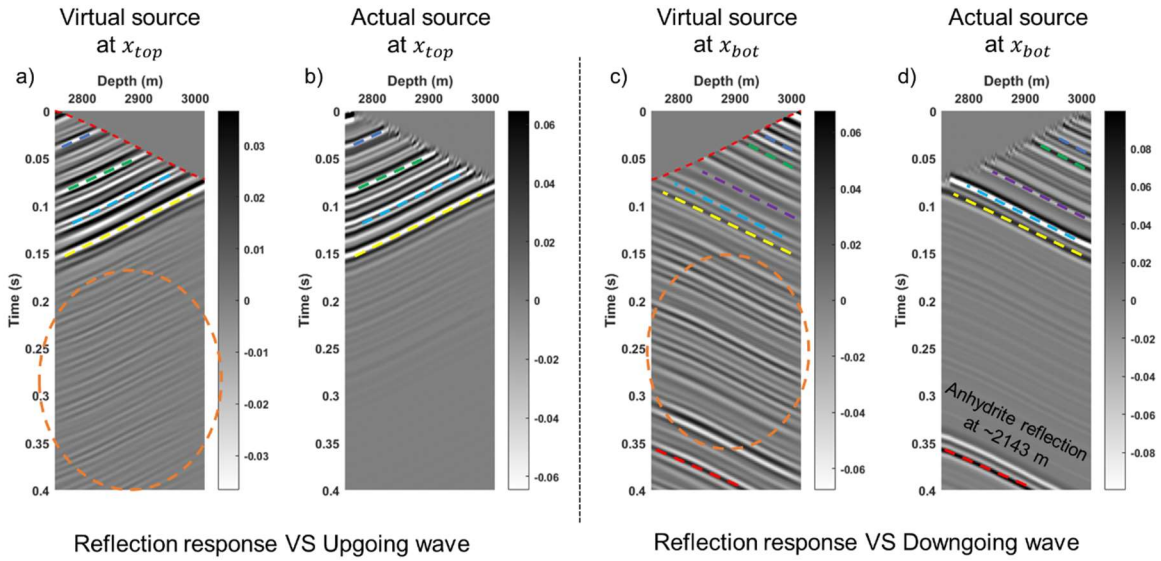

Figure 11 *Reflection response estimation using synthetic shot data. a) and c) are reflection response with a virtual source at the top and bottom geophone. b) The upgoing wave from an actual source at the top geophone. d) Downgoing wave from an actual source at the bottom geophone. Coloured dashed lines represent events in the interferometry result that match with the up- or downgoing events from the model. Dashed circle shows artifacts of spurious arrivals.*

Reflection responses from interferometry and actual upgoing waves from the model are consistent for a source at the top geophone (Fig. 11a and 11b). For a source at the bottom geophone, the estimated reflection response does match some of the actual downgoing waves (Fig. 11c and 11d) but also displays prominent artifacts of spurious arrivals (Snieder et al., 2006; Chen, 2017). This is because there are insufficient upgoing waves from the bottom geophone as the *Vp* log to create the synthetic response is only available up to ~50 meters deeper from the bottom geophone, thus there are not enough reflection interfaces to generate substantial upgoing waves. If deconvolution is applied on the same truncated model as in Fig. 11b or 11d, the deconvolution result and the actual wave are consistent. Despite having prominent artifacts, reflection response estimation with a virtual source at the bottom geophone (Fig. 11c) successfully resolves the strong Anhydrite reflection interface at ~2143 m depth (yellow arrow in Fig. 5).

The transmission response from interferometry displays explicit match with the actual up- or downgoing wave from the model only to the first-order transmission (Fig. 12). Some of the transmission responses at later time only subtly match with the actual wave from the model (colored dashed line). This dissimilarity is due to artifacts in the right side of equation 4 and 5 that is not eliminated by deconvolution. The artifact in this application of seismic interferometry is described in Chapter 7. As in the reflection response estimation, if deconvolution is applied on the same truncated model as in Fig. 12b or 12d, the transmission response and the actual wave are also consistent.

Although containing artifacts of spurious arrivals, plus insufficient input of upgoing wave because of depth limitation of *Vp* log data, deconvolution interferometry using synthetic shot data successfully

estimates the actual reflection and transmission events. Reflection and transmission response estimation using homogenous medium above the top geophone eliminates the artifacts at the wave coda. This heuristic argument supports the existence of spurious events in deconvolution interferometry.

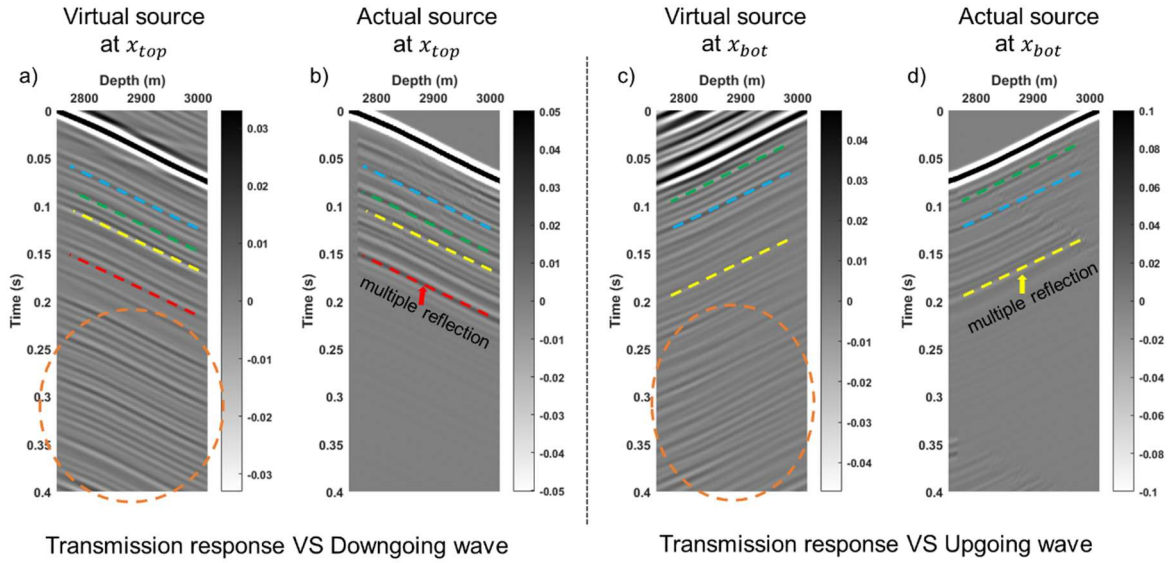

Figure 12 *Transmission response estimation using synthetic shot data. a) and c) are transmission response with a virtual source at the top and bottom geophone. b) The downgoing wave from an actual source at the top geophone. d) Upgoing wave from an actual source at the bottom geophone. Coloured dashed lines represent events in the interferometry result that match with the up- or downgoing events from the model. Dashed circle shows artifacts of spurious arrivals.*

4 Wavefield separation in active and passive field data

The same f-k filtering parameters as in the synthetic shot data is applied to the check shot and noise data. For check shot and noise data, the band-pass filter of 5.5 – 37 Hz is applied prior f-k filtering to suppress aliasing. The data is first resampled to 250 Hz as in the processing sequence in Fig. 6.

Fig. 13 and 14 show the up- and downgoing wave separation process in the f-k domain using check shot and noise data. As in the synthetic data, f-k filtering in check shot data is also unable to fully resolve events at the boundary of the seismic section. The change of slope at the section boundary in Fig. 13a appears linear in Fig. 13b (red dashed line). The f-k filter also introduces artifacts above the first-arrival downgoing wave. These shortcomings of f-k filtering process are expected to affect the deconvolution interferometry result.

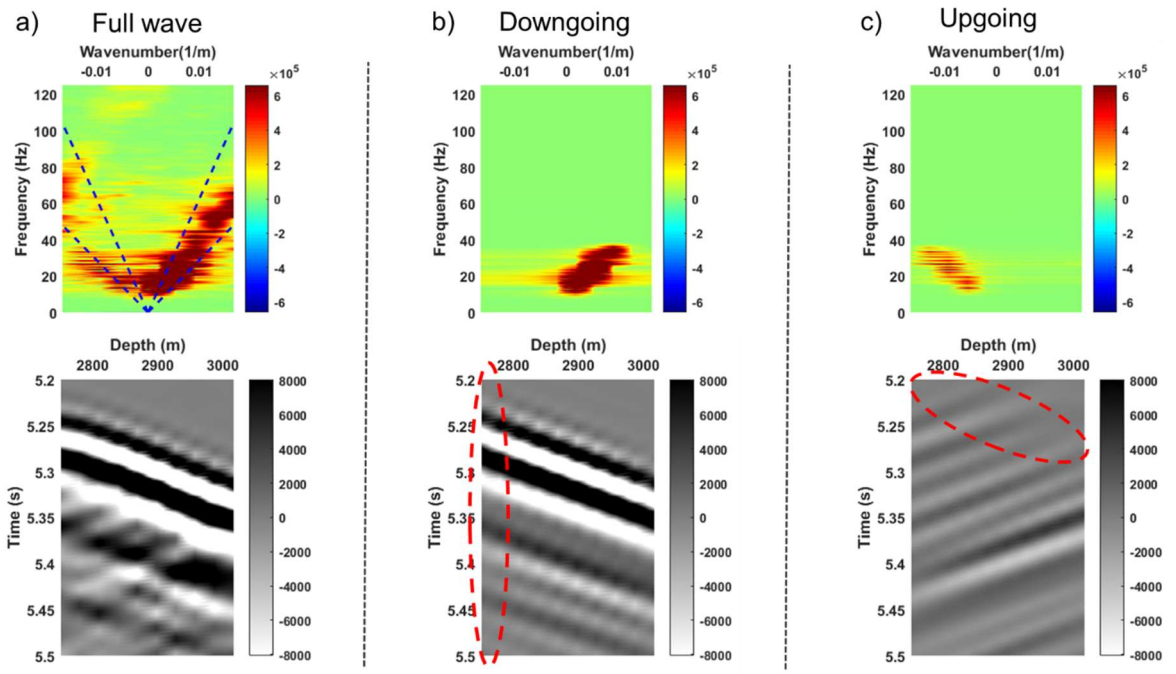

Figure 13 *Wavefield separation of check shot data in the f-k domain. a) The up- and downgoing wave and its f-k spectrum. b) The downgoing wave and its f-k spectrum. Red dashed circle shows poorly resolved events at the seismic section boundary. c) The upgoing wave and its f-k spectrum. Red dashed circle shows area in which contains artifacts of the f-k filter above the first-order downgoing wave.*

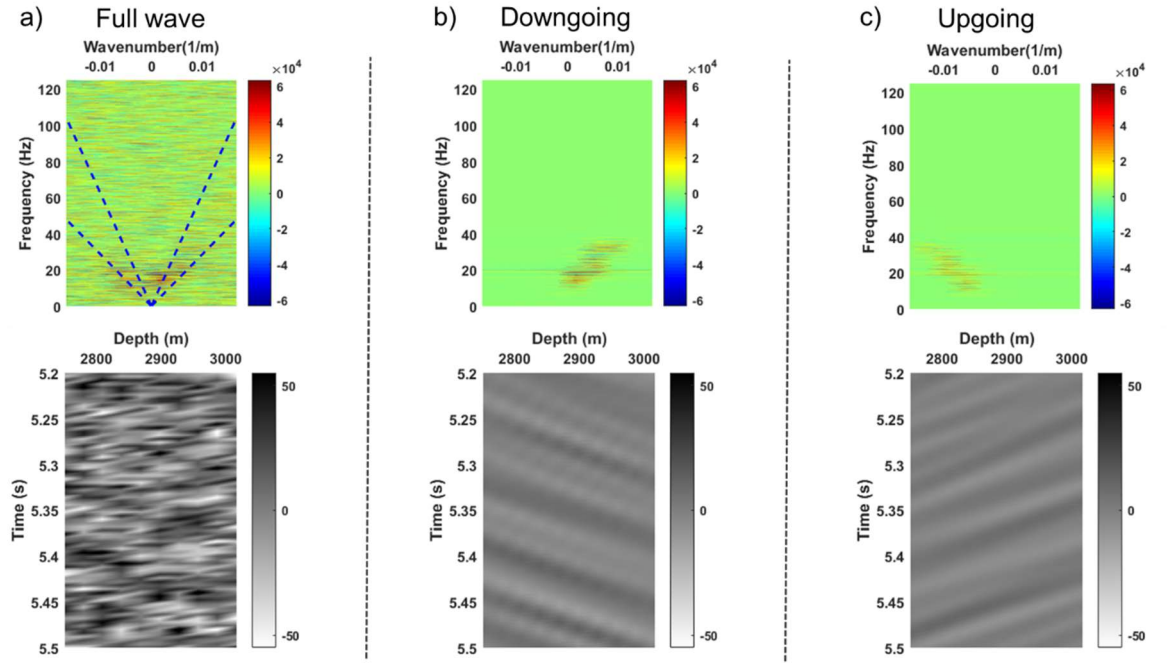

Figure 14 *Wavefield separation of noise data in the f-k domain. a) The up- and downgoing wave and its f-k spectrum. b) The downgoing wave and its f-k spectrum. c) The upgoing wave and its f-k spectrum.*

5 Reflection and transmission response estimation from field data

For check shot and noise data, final transmission and reflection response estimates result from the time integration of the deconvolution using every 30 sec time interval records. A total of 4 check shots records and 2884 noise interval records are used for time integration. Although the check shots are not exactly located above the well, the waves recorded at the geophone array are within the stationary phase region as described in Chapter 6.

5.1 Active field data

Deconvolution interferometry results for check shot data compared with actual up- and downgoing wave from the model are shown in Fig. 15 and 16. Coloured dashed line represents events in interferometry result that match with the actual up- or downgoing wave. Red dashed lines are the first arrivals time based on the well-log *Vp* data. For interpretation convenience, non-physical events above this first arrivals are muted in the reflection response. The corresponding number in some of the lines represents the interpretation of the n-order transmission/reflection wave as it reflected multiple times from two major reflection interfaces at the top and bottom of the reservoir. The actual up- and downgoing wave from the model is using the same truncated 1D elastic model as in Fig. 11b and 12b for a virtual source at the top geophone, and as in Fig. 11d and 12d for a virtual source at the bottom geophone. To make a relevant comparison with a low-frequency signal of check shot and noise data, the up- and downgoing synthetic response are now generated using wavelet with a peak frequency of 18 Hz.

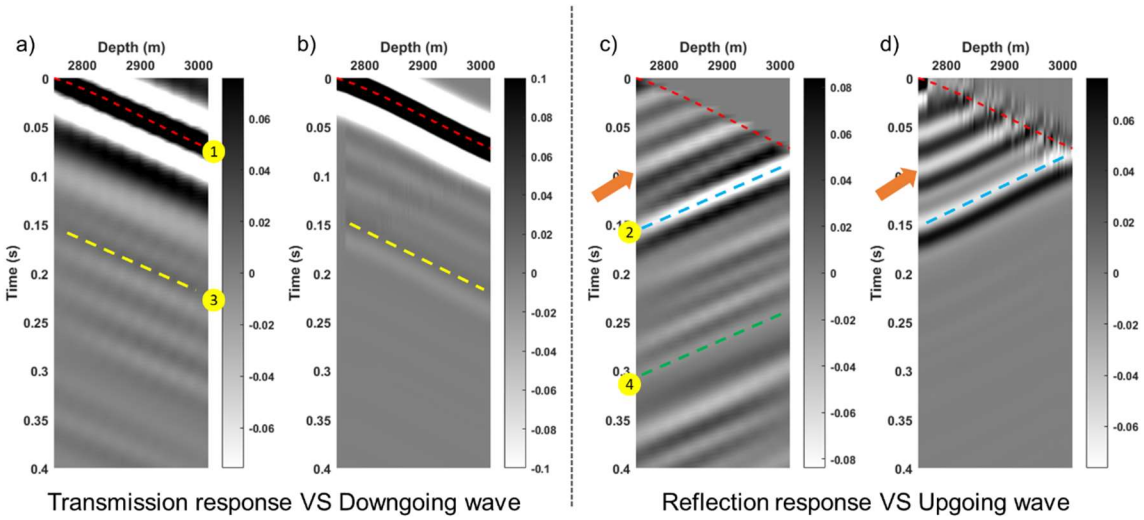

Figure 15 *Interferometry using check shot data for a virtual source at the top geophone. a) and b) are the estimated transmission response and the actual downgoing wave from the model. c) and d) are the estimated reflection response and the actual upgoing wave from the model. The up- and downgoing wave synthetic response is generated from the same truncated model as in Fig. 11b and 12b, except now using 18 Hz peak frequency wavelet.*

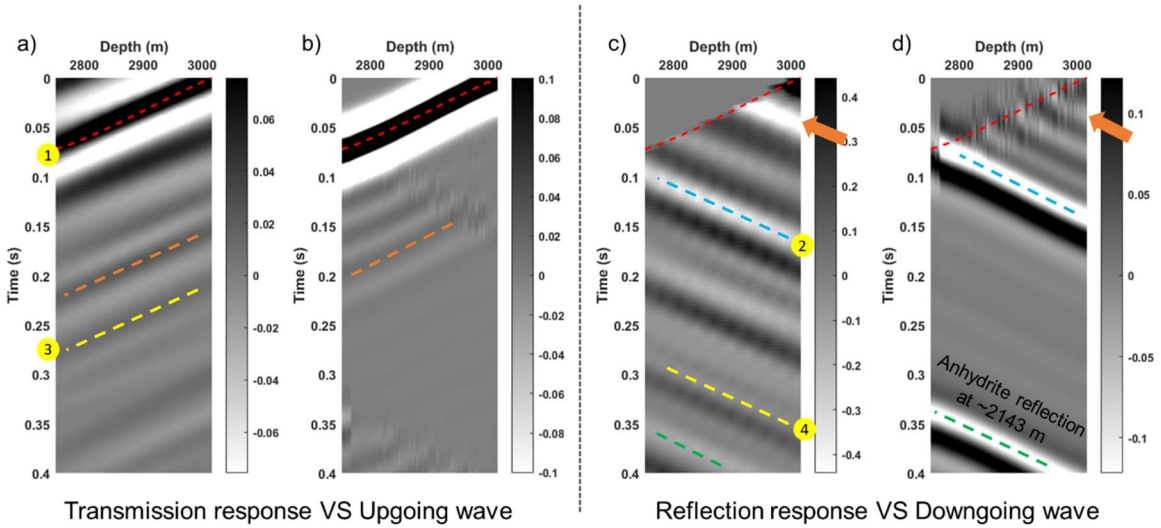

Figure 16 *Interferometry using check shot data for a virtual source at the bottom geophone. a) and b) are the estimated transmission response and the actual upgoing wave from the model. c) and d) are the estimated reflection response and the actual downgoing wave from the model. Up- and downgoing wave synthetic response is generated from the same truncated model as in Fig. 11d and 12d, except now using 18 Hz peak frequency wavelet.*

The first-order transmission response (Fig. 15a and 16a) agrees well with the first arrival travel time based on the *Vp* log (red dashed line). This suggests that deconvolution interferometry can estimate smooth velocity structure in the reservoir.

Fig. 15c shows the reflection response which can be interpreted as the reflected direct arrival (red dashed line) as it meets reflection interface within and around the reservoir. The intersection of the known direct wave arrival times with the reflection events on the gathers provides an estimate of reflection depth. A strong reflection is visible shortly after the first arrival reaches the bottom geophone, indicating that there is a reflection interface not far beneath the bottom geophone. From the *Vp* log, we identify this as a physical reflection from the interface at ~3033 m (grey arrow in Fig. 5) which is the contact interface of the Rotliegend reservoir and the Upper Carboniferous. The estimated transmission and reflection response using a virtual source at the top geophone also indicates what we interpreted as the 1st to 4th-order wave that has reflected multiple times from two major interfaces at the top and bottom of the Rotliegend reservoir (Fig. 15a and 15c).

Unlike Fig. 11c, now by using real data, a strong reflection is visible in Fig. 16c around the top geophone, suggesting a reflector around the top geophone. We identify this as a physical reflection from a thin layer of basal anhydrite at ~2721-2765 m (blue arrow in Fig. 5). With a dominant frequency of 18 Hz and average velocity of 5900 m/s, the general threshold for vertical resolution of 82 m (a quarter of dominant wavelength) is well above the thickness of this layer (~44 m), hence the data cannot resolve both interfaces. Hence, the strong reflection around the top geophone in Fig. 16c is a superposition of two close interfaces of basal anhydrite. The estimated transmission and reflection response using a virtual source at the bottom geophone also indicates what we interpreted as the 1st to 4th-order wave that has reflected multiple times from two major interfaces at the top and bottom of the reservoir (Fig. 16a and 16c).

Both reflection response from a virtual source at the top and bottom geophone (Fig. 15c and 16c) also indicate a reflection at ~2940 m (orange arrow) due to reservoir heterogeneities, although in Fig. 16c the reflections appear to be phase delayed. The phase delay is pronounced at the time difference of 4th-order wave between interferometry result using top and bottom geophone which has ~0.04 sec delay.

Compared with the up- and downgoing wave from synthetic data (Fig. 15b, 15d, 16b, 16d), the estimated reflection response gives a good agreement for a virtual source at the top geophone, but not

for a virtual source at the bottom geophone as it appears to be phase delayed. This suggests that deconvolution interferometry using check shot data can extract the physical reflection response from actual reflection interfaces accurately by using top geophone as a virtual source. As is the case for synthetic data, estimated first-order transmission response using check shot data can approximate the P-wave velocities structure in the reservoir. Despite having spurious-arrival artifacts in its coda, we can subtly follow the 1st to 4th-order transmission/reflection wave that reflected multiple times from two major reflection interfaces at the top and bottom of the reservoir. Note that because the f-k filter cannot resolve velocity changes at the seismic section boundaries, the interferometry result at section boundaries also appears linear instead of having a slope as appears in the synthetic data.

5.2 Passive field data

The same principle and processing parameters are applied using noise data to estimate the transmission and reflection response with a virtual source at the top and bottom geophone (Fig. 17). The estimated transmission responses in Fig. 17a and 17c approximate the first arrivals travel time based on the *Vp* log (red dashed line). Fig. 17b and 17d show that estimated reflection response from noise data are consistent with check shot data. The interpreted 1st to 4th-order wave using noise data also consistent with the interpretation using check shot data, although transmission/reflection events in noise data lack continuity and have smaller amplitude, for instance, the 3rd order wave in Fig. 3a. This could be due to more unstable spectrum distribution in the f-k domain and lower dominant frequency (16 Hz) compared to the check shot, which directly affects the wavefield separation and deconvolution process. The green dashed line in Fig. 17d resembles the strong Anhydrite reflection in Fig. 16d, however, it could also be a spurious arrival as the amplitude is not as strong.

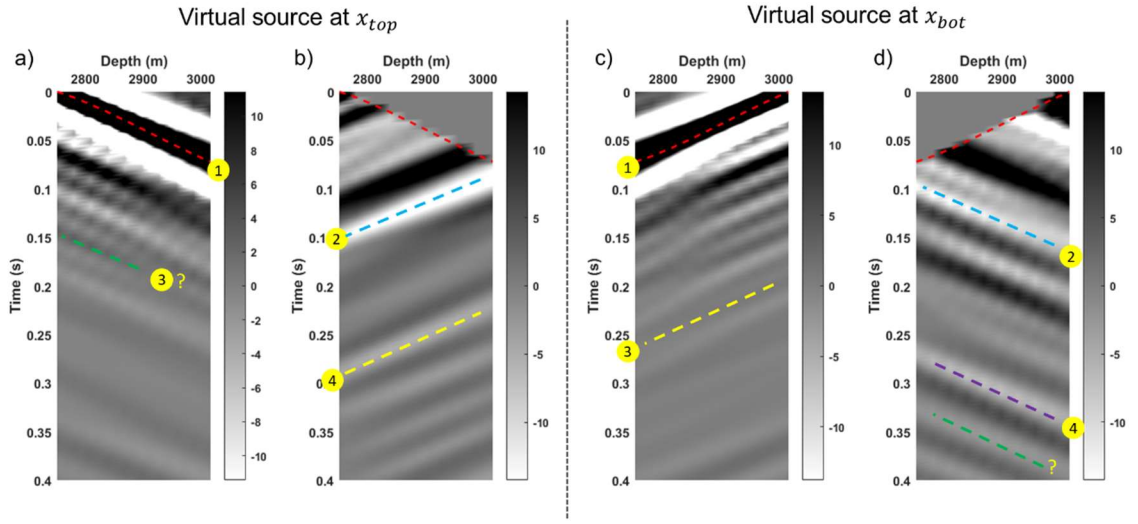

Figure 17 *Interferometry using noise data. a) and b) are the estimated transmission and reflection response for a virtual source at the top geophone. c) and d) are the estimated transmission and reflection response for a virtual source at the bottom geophone.*

The consistency of the results indicates that deconvolution interferometry using noise borehole data can also retrieve the physical reflections and velocity structure in the reservoir. We believe the transmission estimates to be sufficiently accurate with regards to the direct arrivals, but its coda is a superposition of actual transmitted arrivals and artifacts (Vasconcelos et al., 2017). Thus, these non-physical events must be properly accounted for and one must be extra cautious in interpreting the estimated transmission and reflection response.

We have seen that interferometry using active and passive borehole data enables us to obtain reliable subsurface information without the knowledge of the velocity model between the source and geophones, where sometimes conventional methods fail to image the data below complex media (Bakulin &

Calvert, 2006) such as sub-salt flank (Vasconcelos & Snieder, 2008). The interferometry application in this research is using the P-wave from vertical component records only. The same concept is also applicable to the S-wave from the horizontal component of the check shot or noise records. Zhou & Paulssen (2017) approximated the S-wave velocity in the reservoir and furthermore determined azimuthal anisotropy from the S-wave polarizations. High sensitivity to small medium changes in passive borehole interferometry and its high degree of repeatability is useful for reservoir monitoring (Wapenaar et al., 2010; Behm, 2017; Zhou & Paulssen, 2017; Bakulin, 2007). Thus, one can detect the velocity and/or interface variations in the reservoir for time-lapse studies with relatively cheaper cost and less effort compared to conventional approaches. With the identifiable time-lapse change in the reservoir, we can also use it to monitor induced seismicity, which in the Groningen gas field, is mainly caused by gas production (van Thienen-Visser & Breunese, 2015).

6 Stationary phase analysis

One requisite of 1D seismic interferometry is that the wave must come from sources in Fresnel zones around stationary points (Wapenaar et al., 2010). Stationary phase is expected for deep borehole data because even though the check shots are at some distance away from the well at the surface (Fig. 18a), multiples and scattering paths within the medium between the surface and the geophone array are sufficient to deliver almost vertically propagating rays to the array (Fig. 18b).

Stationary phase analysis is performed by deconvolution interferometry at varying time window and duration using SP2 (Fig. 18c) which is the furthest check shot from the well at the surface. Fig. 19 and 20 show the results of every 0.8 sec time window, with 0.6 sec overlap starting from 4.7 sec record. First arrivals travel times in SP2 starts at ~5.24 sec, thus the first time window already includes a small part of the signal. Records prior to the first arrivals consist of noise data only.

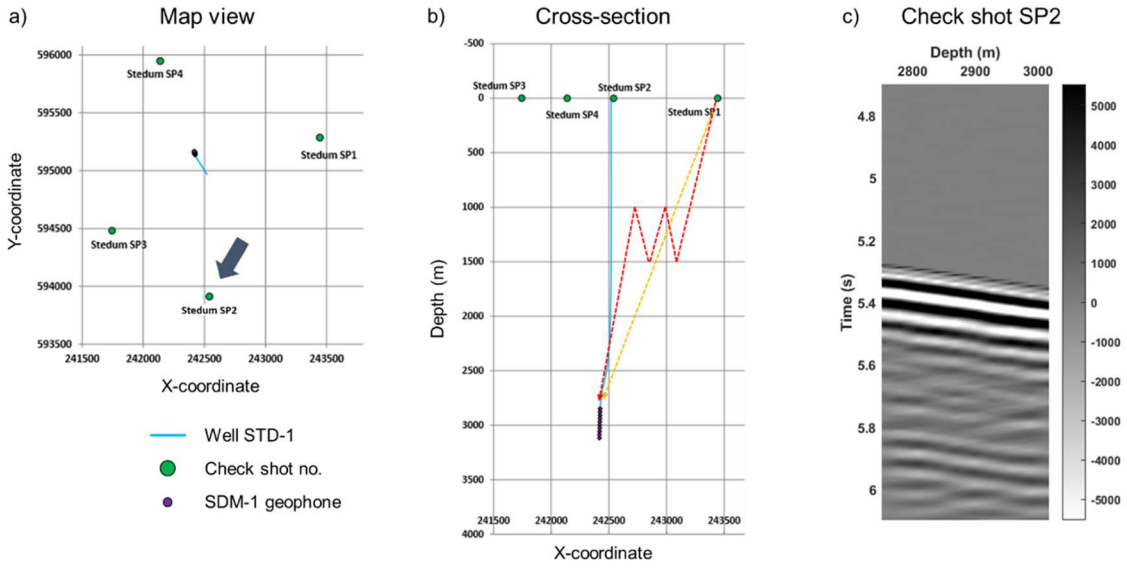

Figure 18 *Four check shot locations around the SDM-1 well. a) Map view of check shot locations. SP2 is the furthest check shot from the well (black arrow). b) The horizontal cross-section of the map view. Ray path with more scattering (red dashed line) arrives at the geophone array with smaller incident angle than a direct ray path from the source (yellow dashed line). c) SP2 check shot raw record that is used for time-varying interferometry. Only 4.7-6.1 sec record is shown from full 30 sec record.*

The transmission responses from time-varying interferometry are exceptionally consistent, thus stationary, no matter which time window and duration we chose from the 30 sec record, so long as we include the signal any time after the first arrivals at 5.24 sec. The reflection wave is only consistent if we input the early time window when it includes strong first arrival and its first strong reflected wave

which has the more stable f-k spectrum and frequency content. At much later time windows (>5,7 sec), f-k and spectrogram analysis display more unstable spectrum distributions. This directly affects the wavefield separation and deconvolution itself. Consistent deconvolution results around first arrival time window suggests that the wave that arrives at the geophone array is within stationary phase region.

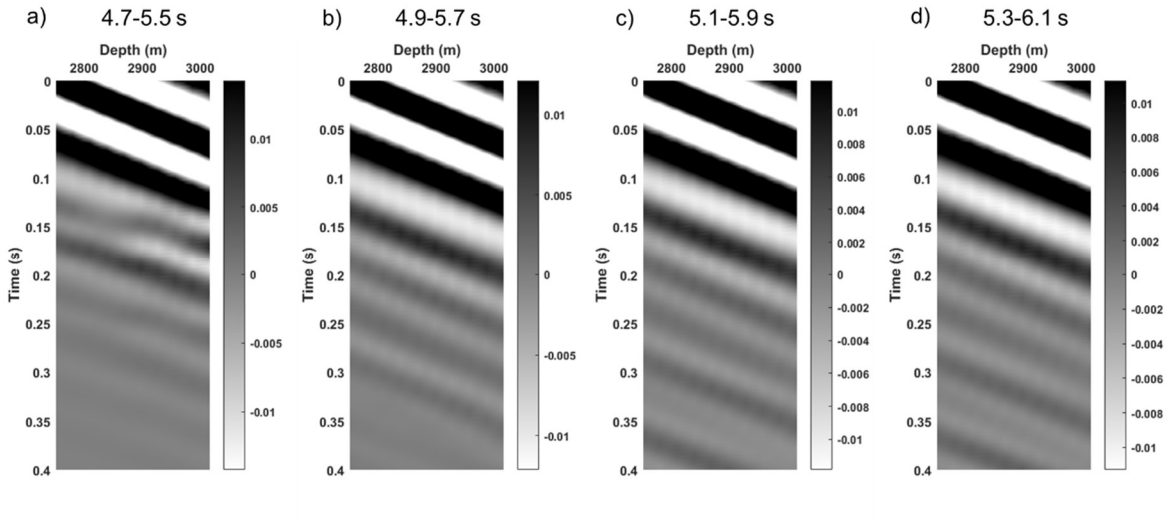

Figure 19 *Transmission response from time-varying interferometry of SP2 check shot. Time above each panel shows the time window of SP2 check shot record used as an input for interferometry.*

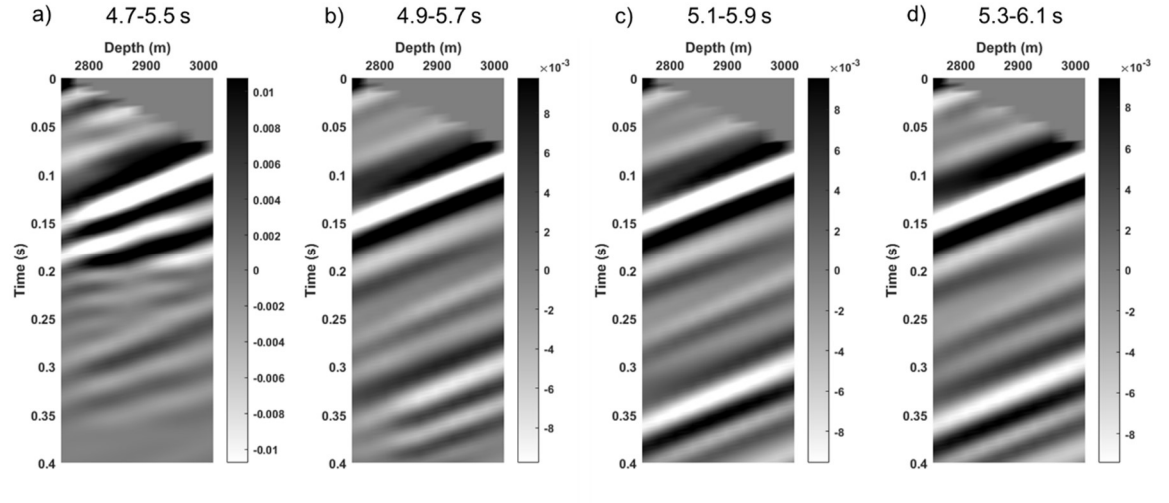

Figure 20 *Reflection response from time-varying interferometry of SP2 check shot. Time above each panel shows the time window of SP2 check shot record used as an input for interferometry.*

7 Artifacts in seismic interferometry

Although sources within the Fresnel zone is sufficient, ideally isotropic illumination is required for seismic interferometry. Isotropic illumination in borehole configuration means the up-down propagation energy is equal, thus the net power flux in the up- and downgoing wave is close to zero (Wapenaar et al., 2010). In our data where the sources originate from the surface, stronger downgoing wave compared to the upgoing wave (Fig. 7) indicates one-sided illumination, hence the amplitudes of energy have a directional variation or irregular illumination. This condition causes incomplete cancellation of contribution from different stationary points which could lead to bias in Green's function retrieval such as the occurrence of spurious arrivals artifact (Wapenaar et al., 2010; Snieder et al., 2006; Chen, 2017) as we have seen in the interferometry results in the synthetic and field data. In one-sided

illumination, energy radiated by interferometric virtual source differs from that radiated by placing a real physical source at the receiver location, which radiates energy in all direction (Vasconcelos & Snieder, 2008). This is partially what causes the difference in the estimated response from interferometry and the actual response from a physical active source in the synthetic data (Fig. 11 and 12).

For the estimated reflection responses, minor artifacts at the coda are more of the consequences of stabilization parameter (ε^2) in the water-level regularized deconvolution to mitigate notches in the spectrum of $\hat{p}(x_S, w)$ in equation 1. The artifact produced by up-down separation in the f-k domain (Fig. 13) and frequency filtering process (Fig. 8) can also contributes to artifact generation in interferometry. For the estimated transmission response, we have seen at the right side of equation 4 and 5 that what we estimate is not only the local, reservoir-only transmission response, but also artifacts resulted from waves that are propagating from the medium below the bottom geophone for a virtual source at the top, and from the medium above the top geophone for a virtual source at the bottom. Hence, the product of the transmission response estimation in this study is a superposition of the local transmission response and the artifacts due to spurious waves from the medium outside the spatial coverage of the geophone array. This is one of the reason of low signal-to-noise ratio in the estimated local transmission responses in Fig. 12. In the reflection response estimation, this type of artifact is not incorporated in the equation because we are not only estimate the local, reservoir-only reflection responses, but also the reflection from the medium outside the spatial coverage of the array (e.g., Anhydrite reflection at ~2143 m depth, Rotliegend-Carboniferous interface below the bottom geophone). Thus, equation 2 and 3 are valid for reflection response estimation. If we are targeting only the local reflection within the reservoir, equation 2 and 3 must also be modified as in the equation 4 and 5 to incorporate spurious artifacts from the medium below the bottom geophone for a virtual source at the top, and from the medium above the top geophone for a virtual source at the bottom.

To minimize interferometric artifacts, Bakulin & Calvert (2006) suggested a solution by applying a time window which aims to select the strong direct waves only as the input. This is the case for Fig. 19 and 20, which are using an input time window within strong first arrivals only. As the result, Fig. 21 shows that it suppresses high-frequency events which could be the frequency content of spurious arrivals artefact (arrow at ~32 Hz). In this study, spurious arrivals from overburden medium are suppressed by the up- and downgoing wavefield separation prior to interferometry (Mehta et al., 2007). However, we have seen that minor spurious arrivals still occur partially due to one-sided illumination characteristic in the field data, furthermore, it is very prominent in the synthetic data for reasons described in Chapter 3.2 and in the previous paragraph.

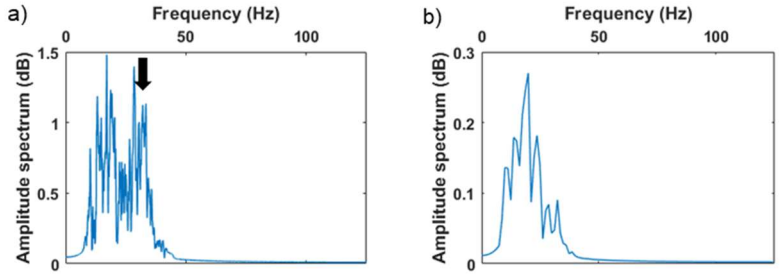

Figure 21 *Frequency content of reflection responses with and without time windowing from a virtual source at the top geophone using check shot data. a) Frequency content of Fig. 15c, which is using a full time window of 30 sec. b) Frequency content of Fig. 20c, which is using a time window selecting only the strong arrivals at 5.1-5.9 sec. The arrow points to what could be the frequency content of the artifact.*

Mehta et al. (2007) and Snieder et al. (2006) suggested that these spurious artifacts are eliminated if sources below the target reflectors are included, thus aiming for isotropic illumination. In deconvolution interferometry, excessive multiple scattering can also potentially extract a response that is closer to full elastic response. Such condition can be met if the geophone array is deep enough, the overburden

medium is highly heterogeneous, and with a long recording time. However, it is difficult to predetermine how long the required recording time that allow for sufficient multiple scattering to compensate the lack of sources (Vasconcelos & Snieder, 2008). When applicable, a more advanced technique to suppress these artifacts is by multi-dimensional deconvolution which not only corrects for irregular source distribution and spurious arrivals due to one-sided illumination, it also improves radiation pattern of the virtual source and accounts for dissipation (Wapenaar et al., 2010).

8 Conclusions

The interferometry application to estimate the reflection and local transmission response in the reservoir requires up- and downgoing P- and S-wave separation as the input. Wavefield separation is performed in the f-k domain and the process is validated using the synthetic responses from the 1D elastic model. Using active and passive deep borehole data, we estimate the full-waveform reflection responses by deconvolution interferometry for a virtual source at the top geophone which is consistent with the actual responses from the synthetic data as if we have an active source at the top geophone. As for virtual source at the bottom geophone, reflection response appears to be phase delayed, though it contains arrivals consistent with the geology. We have shown that the estimated reflection wave is physically meaningful, resulting from actual subsurface reflection interfaces. Using the same principle, a first-order estimated transmission wave yields a direct wave in which the slope corresponds to the P-wave velocity in the reservoir.

However, it is important that in interpreting coda waves from interferometry, non-physical events such as spurious arrival artifacts must be accounted for, or least be considered during interpretation, especially when the source distribution is not isotropic, i.e., when illumination is directionally uneven. In the more extreme cases, one-sided illumination can lead to bias in impulse response retrieval.

Interferometry with time-varying input windows shows that the results are consistent, providing a reliable indication that the waves contributing to the interferometry result are within the stationary phase region. This interferometry application is applicable in similar borehole settings so long as the waves are within stationary phase region, which is one of the requirements in seismic interferometry.

Reliable subsurface information obtained from active and passive borehole interferometry in the Groningen gas field can be of use for reservoir monitoring by detecting velocity and/or interface time-lapse variations, subsurface imaging without requiring the velocity model of the overburden medium nor the medium within the reservoir, and further understanding of the mechanics of seismicity induced by gas extraction with substantially reduced cost and effort compared to conventional approaches.

9 Acknowledgements

I would like to kindly thank Ivan, Hanneke, and Wen for their guidance and deep insight throughout this research. We thank Remco Romijn and NAM for providing the seismic and well-log data. I would like to give my highest regards to my family and colleagues who have always supported me. Appreciation to PPIU (Indonesian Student Association in Utrecht) for being my second home in Utrecht. At last, my sincerest gratitude to LPDP (Indonesia Endowment Fund for Education) for funding my study.

References

Bakulin, A. and Calvert, R., 2006. The virtual source method: Theory and case study. *Geophysics*, *71*(4), pp.SI139-SI150.

Bakulin, A., Mateeva, A., Mehta, K., Jorgensen, P., Ferrandis, J., Herhold, I.S. and Lopez, J., 2007. Virtual source applications to imaging and reservoir monitoring. *The Leading Edge*, *26*(6), pp.732-740.

Behm, M., 2017. Feasibility of borehole ambient noise interferometry for permanent reservoir monitoring. *Geophysical Prospecting*, *65*(2), pp.563-580.

Chen, X., 2017. The modelling and interpretation of borehole data of the Groningen gas reservoir by seismic interferometry. *Utrecht University, Faculty of Geoscience, Department of Earth Science*, Guided Master research.

Curtis, A., Gerstoft, P., Sato, H., Snieder, R. and Wapenaar, K., 2006. Seismic interferometry—Turning noise into signal. *The Leading Edge*, *25*(9), pp.1082-1092.

Liu, Y., Wapenaar, K., van der Neut, J. and Arntsen, B., 2014, October. Combining inter-source seismic interferometry and source-receiver interferometry for deep local imaging. In *2014 SEG Annual Meeting*. Society of Exploration Geophysicists.

Mehta, K., Bakulin, A., Sheiman, J., Calvert, R. and Snieder, R., 2007. Improving the virtual source method by wavefield separation. *Geophysics, 72*(4), pp.V79-V86.

Mehta, K., Snieder, R. and Graizer, V., 2007. Extraction of near-surface properties for a lossy layered medium using the propagator matrix. *Geophysical Journal International*, *169*(1), pp.271-280.

NAM, 2016. Study and data acquisition plan induced seismicity in Groningen – Winningsplan 2016. *NAM report*, (EP201604200072).

Snieder, R., Wapenaar, K. and Larner, K., 2006. Spurious multiples in seismic interferometry of primaries. *Geophysics*, *71*(4), pp.SI111-SI124.

van Thienen-Visser, K. and Breunese, J.N., 2015. Induced seismicity of the Groningen gas field: History and recent developments. *The Leading Edge*, *34*(6), pp.664-671.

Vasconcelos, I., Ravasi, M., Kritski, A., van der Neut, J. and Cui, T., 2017. Local, reservoir-only reflection and transmission responses by target-enclosing extended imaging. In *SEG Technical Program Expanded Abstracts 2017* (pp. 5289-5293). Society of Exploration Geophysicists.

Vasconcelos, I. and Snieder, R., 2008. Interferometry by deconvolution: Part 1—Theory for acoustic waves and numerical examples. *Geophysics*, *73*(3), pp.S115-S128.

Vasconcelos, I. and Snieder, R., 2008. Interferometry by deconvolution: Part 2—Theory for elastic waves and application to drill-bit seismic imaging. *Geophysics*, *73*(3), pp.S129-S141.

Wapenaar, K., Draganov, D., Snieder, R., Campman, X. and Verdel, A., 2010. Tutorial on seismic interferometry: Part 1—Basic principles and applications. *Geophysics*, *75*(5), pp.75A195-75A209.

Wapenaar, K. and Fokkema, J., 2006. Green's function representations for seismic interferometry. *Geophysics*, *71*(4), pp.SI33-SI46.

Wapenaar, K., Slob, E., Snieder, R. and Curtis, A., 2010. Tutorial on seismic interferometry: Part 2—Underlying theory and new advances. *Geophysics*, *75*(5), pp.75A211-75A227.

Zhou, W. and Paulssen, H., 2017, April. Monitoring the Groningen gas field by seismic noise interferometry. In *EGU General Assembly Conference Abstracts* (Vol. 19, p. 3903).

Zhou, W. and Paulssen, H., 2017. P and S velocity structure in the Groningen gas reservoir from noise interferometry. *Geophysical Research Letters*, *44*, pp.11,785–11,791.